

# Robust and Automated Method for Spike Detection and Removal in Magnetic Resonance Imaging

David S. Smith<sup>\*†</sup>, Joel Kullberg, Johan Berglund, Malcolm J. Avison, and E. Brian Welch

December 1, 2021

## Abstract

Radio frequency (RF) spike noise is a common source of exogenous image corruption in MRI. Spikes occur as point-like disturbances of  $k$ -space that lead to global sinusoidal intensity errors in the image domain. Depending on the amplitude of the disturbances and their locations in  $k$ -space, the effect of a spike can be significant, often ruining the reconstructed images. Here we present both a spike detection method and a related data correction method for automatic correction of RF spike noise. To detect spikes, we found the  $k$ -space points that have the most significant effect on the total variation of the image. To replace the spikes, we used a compressed sensing reconstruction in which only the points thought to be corrupted are unconstrained. We demonstrated our technique in two cases: (1) in vivo gradient echo brain data with artificially corrupted points and (2) actual, complex scanner data from a whole-body fat-water imaging gradient echo protocol corrupted by spikes at uncertain locations. Our method allowed near-perfect detection and correction with no human intervention. We calculated Matthews correlation coefficients and sensitivities above 0.95 for a maximum of 0.78% corruption in synthetically corrupted in vivo brain data. We also found specificities above 0.9994.

## 1 Introduction

Radio frequency (RF) spike noise in magnetic resonance imaging (MRI) typically manifests as bursts of high-amplitude corruptions in the Fourier domain ( $k$ -space) that lead to Moiré patterns in the reconstructed image. Spikes originate from brief disruptions in the electromagnetic field near the receive coil during periods when the receiver channel is open during an exam. Common sources are static discharge in clothes, mechanical stress and vibration in the scanner, receive hardware failures, and leaks in the RF shield that permit external RF interference.

Traditional spike detection techniques rely on thresholding based on the RF receive signal amplitude [1, 2], statistical analyses of data [3, 4], or window filters [5]. With the exception of [5], all detection has been performed entirely in  $k$ -space. Detected spikes are then typically replaced by zeros or by local interpolation of  $k$ -space neighbors [1, 2, 4]. In one notable case [5], an analytic solution to the missing data was used.

The recent application of compressed sensing (CS) [6, 7] to MRI has allowed the acquisition of MRI data with a significant relaxation of sampling requirements [8]. In many cases, CS techniques can allow for reconstruction of full MRI data sets from just 25% or less of the full data set, as would historically be defined by the Nyquist-Shannon sampling theorem. The ephemeral nature of

---

<sup>\*</sup>Institute of Imaging Science and Department of Radiology and Radiological Sciences, Vanderbilt University Medical Center, Nashville, TN

<sup>†</sup>Corresponding author: david.smith@vumc.org

RF spikes, which leads to local corruption of the  $k$ -space data, suggests that a CS reconstruction of the corrupted data should be extremely accurate.

We were initially motivated to find an improved spike detection and removal algorithm because we experienced severely corrupted data in a longitudinal fat-water imaging study. The data were taken with a faulty RF room shield, and the built-in commercial software was unable to correct the severely corrupted data on a majority of slices. In this work, we present our resulting improved and robust methods for both spike detection and removal that require no user intervention or prior information about the acquisition of the data. This method can also be run retrospectively when post processing already acquired data.

In Section 2, we describe a new method for spike detection and removal. In Section 3, we show the results of this method on both in vivo brain data with synthesized spikes and severely corrupted actual whole-body gradient echo data, acquired with a damaged RF room shield beneath the patient support and containing an unknown number of spikes arising from RF leakage secondary to loss of RF shield integrity. In Section 4, we discuss the practical uses for our methods and possible improvements.

## 2 Materials and Methods

### 2.1 Spike Detection Method

During collection of the data at an MRI scanner, the imaging volume is encoded by variable spatial frequencies that are then interpreted as the coefficients of the discrete Fourier transform (DFT) of the target. Perturbing a single Fourier coefficient in  $k$ -space will lead to global sinusoidal intensity variations in the image. In one sense, the coefficients of the DFT are the coefficients which minimize the approximation error of the imaging target. Since anatomical structures are typically smooth objects on a flat (signal free) background, the coefficients that cause the most “rippling” in the image should be the least accurate. Furthermore, since all coefficients are corrupted at some level by noise, we would like to distinguish a point of diminishing returns, beyond which we are replacing noisy, but probably valid, data. Optimal image improvement should result when all data corrupted by RF spikes are replaced and all valid points are retained. In practice, however, this may not necessarily be possible, so we must plan to strike a balance between possibly missing spikes and not correcting all image artifacts or possibly discarding valid data and losing the information that it contained.

We define the collected data, or  $k$ -space, of a complex-valued image  $\mathbf{x}$  as  $\mathbf{d} = \mathcal{F}\mathbf{x}$ , where  $\mathcal{F}$  is the DFT operator. To begin spike detection, each element of  $\mathbf{d}$  was zeroed in turn, and a corresponding modified magnitude image  $\mathbf{x}^k$  was created with an inverse DFT:

$$\mathbf{x}^k = |\mathcal{F}^{-1}\mathbf{I}^k\mathbf{d}|, \quad (1)$$

where  $\mathbf{I}^k$  is the identity matrix with the  $k$ -th element along the diagonal set to zero. In theory, if the datum  $d_k$  deleted was valid, the image quality of  $\mathbf{x}^k$  should decrease; if  $d_k$  had been corrupted, the image quality should improve. Since the total variation (TV) is very sensitive to alterations in the Fourier domain, we hypothesized that the TV should separate the corrupted data from the valid data.

A vector of aggregated TV values  $\mathbf{t}$  was then constructed, where the  $k$ -th element of  $\mathbf{t}$  was computed as the TV of the derived image  $\mathbf{x}^k$ :

$$t_k = \sum_{s=1}^N \left\| \nabla_s \mathbf{x}^k \right\|_1, \quad (2)$$

where  $N$  is the total number of data points,  $\nabla_s$  is the forward difference along the dimension  $s$  (e.g.  $s = \{1, 2, 3\}$  for a 3-D protocol) and  $\|\cdot\|_1$  is the  $\ell_1$ -norm, defined for a vector  $\mathbf{v}$  as  $\|\mathbf{v}\|_1 = \sum_i |v_i|$ .

Next, the upper half of  $\mathbf{t}$  was assumed to be valid and were discarded (these points had the least effect on image total variation). The remaining  $\mathbf{t}$  values were retained and normalized to lie between 0 and 1. Then a threshold  $\theta$  was selected using Otsu’s method [9] (see, e.g., Fig. 2). Since the penalty in terms of image quality is more severe when corrupted data is missed than when clean data is thought to be corrupted, we increased the cutoff between corrupted and clean data to  $\sqrt{\theta}$  (recall that  $\mathbf{t}$  has been normalized to be between zero and one). This provided a more aggressive selection of spiked data and will be shown below to be the most robustly accurate method.

All  $\mathbf{t} < \sqrt{\theta}$  were assumed to be spikes. The suspected spikes were then discarded to create a data constraint mask  $\mathbf{M}$  for the reconstruction:  $\mathbf{M} = \prod_{\hat{k}} \mathbf{I}^{\hat{k}}$ , where  $\hat{k} \in \{k : t_k < \sqrt{\theta}\}$ . The spike detection algorithm is listed in Algorithm 1.

---

**Algorithm 1** :: Spike Detection

---

**Require:** input data  $\mathbf{d}$

**for all** data points  $k$  **do**

$\mathbf{g} \leftarrow \mathbf{d}$

$g_k \leftarrow 0$

$t_k \leftarrow \text{TV}(\mathcal{F}^{-1}\mathbf{g})$

**end for**

Discard upper half of  $\mathbf{t}$ .

Normalize remaining  $\mathbf{t}$  to lie on  $[0, 1]$  interval.

Calculate Otsu threshold  $\theta$  for  $\mathbf{t}$ .

All  $\mathbf{t} < \sqrt{\theta}$  are labeled as assumed spikes.

**return**

---

## 2.2 Collection of Real Data Free of Spikes

First, a gradient echo data set was used that was free of spikes to use as a baseline for adding synthetic spikes. This gave us a benchmark for accuracy testing of the algorithm. This data was acquired on a Philips 7T scanner with an axial field of view (FOV) of 256 mm  $\times$  256 mm and an in-plane voxel size of 1 mm  $\times$  1 mm. The slice thickness was 2.5 mm. The flip angle was 35 deg, and no partial Fourier or parallel imaging was used. The TE1/ $\Delta$ TE/TR was 1.74/2.3/200 ms. Total scan time for the acquisition of 32 echoes was 205 s. A reconstructed matrix size of 256<sup>2</sup> was produced by gridding 512 radial profiles. This gridded Cartesian data was inverse transformed to produce a 256  $\times$  256 Cartesian image. This final, complex image was our baseline “clean” image that synthetic spikes were then added to for the synthetic spike corruption experiment.

## 2.3 Collection of Real Data Corrupted by Spikes

As a real-world application, we applied the algorithm to gradient echo data from an *in vivo* fat-water MRI protocol. For this acquisition, the subject entered a dual-transmit Philips 3.0 T Achieva TX scanner (Philips Healthcare, Best, The Netherlands) feet-first in a supine position with arms extended above the head. The integrated quadrature body coil was used for both transmit and receive. A multi-station protocol with 20 table positions was used to acquire whole-body data. Each of the 20 stacks consisted of a multi-slice, multiple gradient echo acquisition with 12 contiguous 8 mm slices (240 slices total). Other acquisition details include: TR/TE1/TE2/TE3 [ms] =

75/1.34/2.87/4.40; flip angle 20°; water fat shift = 0.325 pixels (BW = 1335.5 Hz/pixel); axial FOV = 500 mm × 390 mm, acquired matrix size = 252 × 195; acquired voxel size = 2 mm × 2 mm × 8 mm. First-order shimming was performed for each slice stack. The total duration of data acquisition was 4 minutes and 16 seconds. Approximately 5 minutes of additional time was needed for table movement, preparation phases at each table position, and for breath holding pauses. Breath holding was performed for table positions covering the waist to the shoulders.

Reconstruction of water and fat images from the acquired multi-echo data was performed using a generalized three-point Dixon approach [10] in which two solutions were found analytically in each voxel. Fat and water signal components were found by least squares fitting after the true solution was identified by imposing spatial smoothness in a 3D multi-seeded region growing scheme with a dynamic path that allowed low confidence regions to be solved after high confidence regions were solved.

## 2.4 Reconstruction of Corrected Images

Images cleaned of spikes were then reconstructed using an unconstrained TV-regularized compressed sensing reconstruction that iteratively solved the following optimization problem:

$$\mathbf{x}_{\text{clean}} = \arg \min_{\mathbf{x}} \text{TV}(\mathbf{x}) + \frac{\lambda}{2} \|\mathbf{M}\mathcal{F}\mathbf{x} - \mathbf{M}\mathbf{d}\|_2^2, \quad (3)$$

where  $\lambda$  is a scalar weighting factor that controls the balance between promoting sparsity of the gradient image and fidelity to the measured non-spiked data. (The total variation is the  $\ell_1$ -norm of the gradient image.) For the results here,  $\lambda$  was chosen to be high enough that excessive smoothing of the images was avoided; e.g.,  $\lambda = 50$  for unit-normed data. Since we only tested this on Cartesian data, we were able to use a fast split Bregman solver [11] to solve the reconstruction in Eq. 3. The reconstruction code was adapted to run on a compute server with graphics processing unit (GPU) acceleration using Jacket 2.2 (AccelerEyes, Atlanta, GA) and MATLAB R2012a (MathWorks, Natick, MA).

## 3 Results

### 3.1 Application to Data Synthetically Corrupted

We first applied the spike detection algorithm to a clean gradient echo data set of a healthy brain. This data set was originally spike free to the best of our knowledge. To simulate the effect of spiking on the data set in a situation in which the positions of the spikes were known, we added varying numbers of synthetically generated spikes to this data. Random locations in the  $k$ -space data were replaced with spikes with magnitudes equal to the DC coefficient and a phases randomly chosen between 0 and  $2\pi$ . Real spikes can, and probably will, have varying amplitudes, but choosing to fix the magnitude allowed us to concentrate on the detection accuracy in controlled conditions. For example, spikes of smaller magnitude would have been harder to detect, but they also would have a smaller influence on image quality, so the penalty for not detecting them would be smaller. Rather than explore the full problem space of possible spike forms, we chose a simple case for this test. The detection and correction required 7.4 s per case on a GPU-accelerated workstation.

The spike locations, corrupted images, and cleaned images are shown in Fig. 1 for two cases: (1) the case with the largest number of spikes that still achieved perfect recovery, and (2) the case with the worst corruption in which a low-frequency datum was corrupted and our algorithm failed to recover it correctly. While Case 2 appears to be a failure of the algorithm, it was notably a

case with 404 spikes. Case 1 was corrupted by 243 spikes and still achieved perfect recovery. One can see by comparing the middle images of each row in Fig. 1 to the rightmost images how stark the difference is between the corrupted and recovered images and how dramatically the algorithm cleans up the corrupted images.

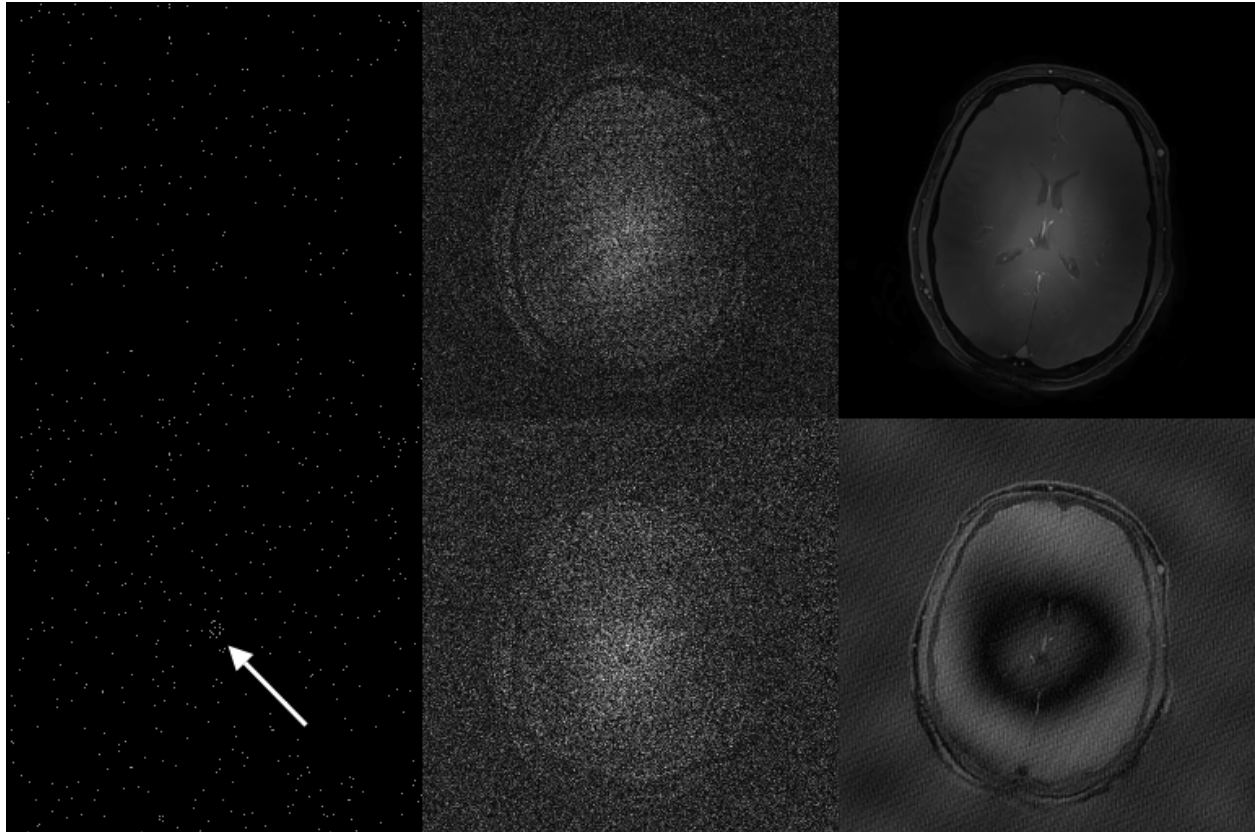


Figure 1: Two examples of 7T brain gradient echo images with synthetic spikes added. The first (top row) is the case with the largest number of spikes (243) that still achieved a perfect reconstruction. The second case (bottom row) was the most severely corrupted case, with 404 spikes added. In this case, the algorithm labeled several points at low spatial frequencies as spikes (arrow), and the severe image artifact can be seen to be a very low spatial frequency feature. This suggests that some of the points deleted and replaced were in fact valid and that they were incorrectly replaced.

A demonstration of the way in which the algorithm separates spikes from genuine data is shown in Fig. 2. Here the lower half of the TV has been normalized and plotted in a histogram. The vertical dashed line is placed at the cutoff  $\sqrt{\theta}$ . Data that, when zeroed out, produce TV values less than the cutoff—to the left of the dashed line—are suspected spikes. Points to the right of the line are assumed to be correct. The histogram shows a bimodal distribution of TV values: a broad distribution at low values and a very narrow, highly peaked distribution near unity. Otsu’s method chooses a TV cutoff value that minimizes the variance between these two distributions, but the histogram suggests that both distributions have overlapping tails, and hence the detection algorithm will in case with many spikes incorrectly label some valid points as spikes and spikes as valid. The goal is to minimize the number of such misclassifications, and Otsu’s method is well suited to that goal.

To quantitatively evaluate the performance of our spike detection algorithm, we measured the

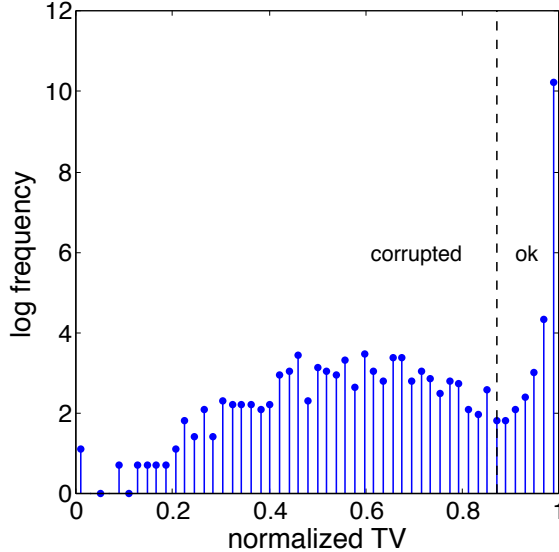


Figure 2: Total variation histogram produced when synthetic spikes were added to 7T gradient echo brain data. Only the lower half of TV values are retained, and then Otsu’s method is performed to determine a cutoff below which points are considered to be spike corrupted.

sensitivity, specificity, and Matthews correlation coefficient of the algorithm as the number of synthetically generated spikes increased using four different exponents for the Otsu’s method cutoff:  $1/p$ , where  $p = \{1, 2, 3, 4\}$ . The results are shown in Fig. 3. The sensitivity and specificity can be written as  $TP/(TP + FN)$  and  $TN/(TN + FP)$ , respectively, where TP is the number of true positives, TN is the number of true negatives, FP is the number of false positives, and FN is the number of false negatives.

Since spike corruption tends to affect only a small fraction of the data set, the usual measure of detection accuracy, defined as  $(TP + TN)/\text{total points}$ , is unreliable. Instead we choose to present the Matthews correlation coefficient (MCC) of the classifications produced by the algorithm (Fig. 3c). The MCC can be thought of as a correlation coefficient between the measured and predicted classification of each point (corrupted or ok). The MCC can be calculated as

$$\text{MCC} = \frac{TP \times TN - FP \times FN}{\sqrt{(TP + FP)(TP + FN)(TN + FP)(TN + FN)}}.$$

We found that all three measures decline as more spikes were added, presumably because the number of real points that randomly had low TV values increased. Sensitivities were very uniformly high ( $> 0.95$ ) for  $p > 1$ . The worst sensitivity was 0.85 for  $p = 1$  at 404 spikes added.

The specificity of the technique is uniformly very high ( $> 0.999$ ) no matter how many spikes were added or the exact value of  $p$ . This is because the vast majority of data points were never selected, and even a few false positives are insignificant compared to the total number of data points.

Finally, the MCC was above 0.9 for all  $p$  up to the maximum number of spikes, but  $p = 2$  was the highest at moderate to high spike corruption levels. For very small numbers of spikes,  $p = 1$  produced a higher MCC, but all  $p$  produced high coefficients ( $> 0.98$ ) at low corruption levels. Since correcting data sets with higher levels of spike correction is a more difficult problem, we believe that  $p = 2$  is the best choice. This has suggested the choice of  $\theta^{1/2}$  for the cutoff, which we adopt throughout.

### 3.2 Application to Data Corrupted by Real Spikes

Next, to test Algorithm 1 under real-world conditions with spikes at uncertain locations, we applied it to *in vivo* whole-body fat-water imaging gradient echo data acquired with a damaged RF room shield. RF interference had severely corrupted the data on almost every slice. These data were corrected using Algorithm 1 and then passed to a fat-water separation algorithm [10] to compare the effects of the data scrubbing on derived quantitative parameters. Data from each echo time were processed separately. The total processing time necessary to correct all slices and echoes of this data set was approximately 30 min on a GPU-accelerated workstation using MATLAB R2012a (MathWorks, Natick, MA).

While the provenance of individual  $k$ -space points cannot be fully known in this case, visually the data appeared to contain hundreds of spikes spread across 240 slices. An example slice containing spikes is shown in Fig. 4. Algorithm 1 automatically detected scores of inconsistent points and eliminated them. The resulting reconstructed images were dramatically improved, and as a side-effect many places throughout the derived fat-water images where water and fat fractions were swapped were corrected. This suggests that spike corruption can have a significant effect on derived image quantities. The histogram of TV values produced is shown in Fig. 5. With a much smaller number of spikes in this case, the form of the distribution is not as clear, but the cutoff produced by the algorithm seems to separate the relatively few number of corrupt points from the much more numerous valid points. The resulting images are shown in Fig. 6. Not only were corrupted points correctly located, but they were replaced with enough accuracy to improve the separation of water and fat in the imaging data.

We measured the artifact level reduction as the mean image magnitude in the region outside of the body. When the spikes were replaced with zeros, we found a 42% decrease in the artifact level outside the body. When a CS reconstruction was used to replace the points, we found a 47% decrease in artifact level.

## 4 Conclusion

We have shown a method for detecting and eliminating radio frequency spikes in MRI data that is automated, robust, and extremely accurate. We demonstrated the success of the technique on both synthetic corrupted data with known spikes and on whole-body gradient echo data corrupted by real RF spike noise. Our method achieved markedly improved images in both cases, and in the *in vivo* experiment also improved the derived fat and water images.

The most significant contribution of Algorithm 1 is the ability to detect corrupted  $k$ -space locations without human intervention. Whatever the source of error,  $k$ -space data that is inconsistent should produce a large effect on the image total variation, a feature that can be exploited to clean images by filtering out corrupted  $k$ -space data. Humans are excellent pattern recognizers, but requiring human intervention is slow and expensive. While Fourier coefficient thresholding certainly works in many cases, it is easy to show an example in which the spikes do not cross the threshold or where the assumptions about the falloff of complex coefficients at high spatial frequencies is incorrect. In fact, the real spike experiment shown here was made possible only because the spiking in this case was missed by the MRI scanner’s commercial built-in algorithm that uses Fourier amplitude thresholding.

The second step of the algorithm, to reconstruct the corrupted data with compressed sensing, is actually only a small (11% relative) improvement over replacing the spiked data with zeroes, but it demonstrates the ability of CS to accurately estimate missing data. The use of CS is justified here because the points deleted were chosen because of their effect on the TV, and CS replaces data

such that the TV effect is minimized. Given the small effect of CS, though, we stress that detection and replacement of spikes, even with zeroes, is more important than implementing the ability to reconstruct the missing data with CS. We choose to show the CS results here for completeness.

Our algorithm does not blur or excessively smooth the image, as can occur with TV-based denoising. Since we are only undersampling the image by a very small amount in  $k$ -space, the data constraint is enforced in the Fourier domain, and we are not affecting the image as much as image-domain techniques like TV denoising. In fact, the amount of data altered here is so slight that only the sinusoidal ripples were removed, and even the background Rician noise in the magnitude image was left intact.

We note that the artifacts due to spiking are coherent and structured, but CS still works perfectly. The literature of compressed sensing MRI frequently refers to the requirement that image artifacts due to the random undersampling be “incoherent,” but this is somewhat incorrect. CS theory states that the measurement basis and the sparse basis should be incoherent, in this case the image gradient and the Fourier measurement. This allows the sparse basis to maximally constrain the data in the measurement domain, effectively turning a global effect into information about single  $k$ -space points. In fact, in the case of RF spike noise with one spike, the image artifact will be extremely coherent, consisting of just one frequency, but TV minimization works extraordinarily well to eliminate it because a single errant point in  $k$ -space produces a global effect on the gradient image.

While Algorithm 1 appears to be robust and flexible, many improvements could be added to increase its accuracy and sensitivity. For example, inconsistencies across multiple receive coil channels or dynamic acquisitions could supplement detection criteria to increase accuracy, perhaps by comparing the variance of  $k$ -space points across time or coil. Most functional MRI and diffusion tensor imaging studies acquire dozens or hundreds of sequential dynamic images with echo-planar readouts that are demanding of gradient hardware and that can frequently cause spiking. The advantage of the large number of dynamics acquired in these studies is that each  $k$ -space location is acquired many times, allowing temporal correlations and statistical methods to be added to the basic TV method presented here. Presumably, the spike distribution would be broader with a higher mean in the histogram of temporal variances for each point. Otsu’s method could determine a separation threshold based on this criteria instead of the TV value alone, or perhaps both could be included in the categorization criteria.

Also, contiguous data samples instead of single  $k$ -space points could be deleted. Because spike occurrence is a temporal phenomenon and  $k$ -space is traversed through time, portions of  $k$ -space larger than a single point may be corrupted by a single RF event. The data in Fig. 4 show an example of this: the bright spikes are clustered and trail along the vertical (readout) axis. In the future, this could possibly be exploited to improve detection accuracy.

If  $k$ -space locations were considered in pairs or larger groups, as well as in isolation, the detection might be improved. The computational penalty for this would be large, however, since each comparison requires a full 2D or 3D fast Fourier transform. Note that examples shown here are 2D only, and moving to a full 3D treatment would be significantly more computationally intensive, but not impossible.

With different data corruption models, this approach could even be extended to motion compensation, Nyquist ghosting, pulsatile artifacts, etc., in which entire readout lines are corrupted or have a systematic error. In these cases, the image TV could constrain the replacement of entire readout lines or help constrain empirical fits in parametric models, such as in the case of gradient delay estimation. However, it is important to note that the concept of identifying inconsistent or corrupted lines of  $k$ -space caused by motion or other sources of data perturbation is not novel. Many methods are described in the literature to detect and compensate for artifacts caused by such



k-space corruption including (but not limited to) dedicated navigator echoes [12, 13], self-navigation [14, 15], iterative autofocusing [16, 17], and methods based on the data redundancy afforded by multi-channel receive coils [18, 19, 20].

The ultimate goal of this type of approach is to create an automated data post-processing step that detects and eliminates RF spikes and creates a “clean”  $k$ -space for the reconstruction pipeline. The method presented here is compatible with a reconstruction post-processing pipeline that works with little or no user intervention to clean up data. Additionally, Algorithm 1 could be modified to aid quality control checks of clinical systems and monitor hardware function. Finally, we have provided evidence here that with an effective spike detection and correction method, discarding a data set due to spiking artifacts may rarely be necessary.

## Acknowledgments

Financial support from NIBIB T32 EB001628 and NCI R25CA092043, NCATS UL1 TR000445.

## References

- [1] M Staemmler and K Gersonde. Echo shape analysis and image size adjustment on the level of echoes: improvement of parameter-selective proton images. *Mag Reson Med*, 3(3):418–24, June 1986.
- [2] T F Foo, N S Grigsby, J D Mitchell, and B E Slayman. SNORE: spike noise removal and detection. *IEEE Trans. Med. Imag.*, 13(1):133–6, January 1994.
- [3] X Zhang, P F Van De Moortele, J Pfeuffer, and X Hu. Elimination of k-space spikes in fMRI data. *Mag Reson Imag*, 19(7):1037–41, September 2001.
- [4] S Chavez, P Storey, and S J Graham. Robust correction of spike noise: application to diffusion tensor imaging. *Mag Reson Med*, 62(2):510–9, August 2009.
- [5] Y H Kao and J R MacFall. Correction of MR kappa-space data corrupted by spike noise. *IEEE Trans. Med. Imag.*, 19(7):671–80, July 2000.
- [6] E J Candès. Compressive sampling. *Proc Intl Cong Mathematicians*, 17(4):295–303, 2006.
- [7] D L Donoho. Compressed sensing. *IEEE Tran Inf Theory*, 52(4):1289–1306, 2006.
- [8] Michael Lustig, David L Donoho, Juan M Santos, and John M Pauly. Compressed Sensing MRI. *IEEE Sig Proc Mag*, 25(2):72–82, 2008.
- [9] Nobuyuki Otsu. A threshold selection method from gray-level histograms. *IEEE Trans. Systems, Man, and Cybernetics*, 9(1):62–66, 1979.
- [10] Johan Berglund, Lars Johansson, Håkan Ahlström, and Joel Kullberg. Three-point Dixon method enables whole-body water and fat imaging of obese subjects. *Mag Reson Med*, 63(6):1659–68, June 2010.
- [11] T Goldstein and S Osher. The split Bregman method for L1-regularized problems. *SIAM J Imag Sci*, pages 1–21, 2009.

- [12] R L Ehman and J P Felmlee. Adaptive technique for high-definition MR imaging of moving structures. *Radiology*, 173(1):255–63, October 1989.
- [13] Anja C S Brau and Jean H Brittain. Generalized self-navigated motion detection technique: Preliminary investigation in abdominal imaging. *Magnetic Resonance in Medicine*, 55(2):263–70, February 2006.
- [14] J G Pipe. Motion correction with PROPELLER MRI: application to head motion and free-breathing cardiac imaging. *Magnetic Resonance in Medicine*, 42(5):963–9, November 1999.
- [15] E Brian Welch, Phillip J Rossman, Joel P Felmlee, and Armando Manduca. Self-navigated motion correction using moments of spatial projections in radial MRI. *Magnetic Resonance in Medicine*, 52(2):337–45, August 2004.
- [16] D Atkinson, D L Hill, P N Stoye, P E Summers, and S F Keevil. Automatic correction of motion artifacts in magnetic resonance images using an entropy focus criterion. *IEEE transactions on medical imaging*, 16(6):903–10, December 1997.
- [17] A Manduca, K P McGee, E B Welch, J P Felmlee, R C Grimm, and R L Ehman. Autocorrection in MR imaging: adaptive motion correction without navigator echoes. *Radiology*, 215(3):904–9, June 2000.
- [18] M Bydder, D J Larkman, and J V Hajnal. Detection and elimination of motion artifacts by regeneration of k-space. *Magnetic Resonance in Medicine*, 47(4):677–86, April 2002.
- [19] David J Larkman, David Atkinson, and Jo V Hajnal. Artifact reduction using parallel imaging methods. *Topics in magnetic resonance imaging : TMRI*, 15(4):267–75, August 2004.
- [20] David Atkinson. Incoherent artefact correction using PPI. *NMR in biomedicine*, 19(3):362–7, May 2006.

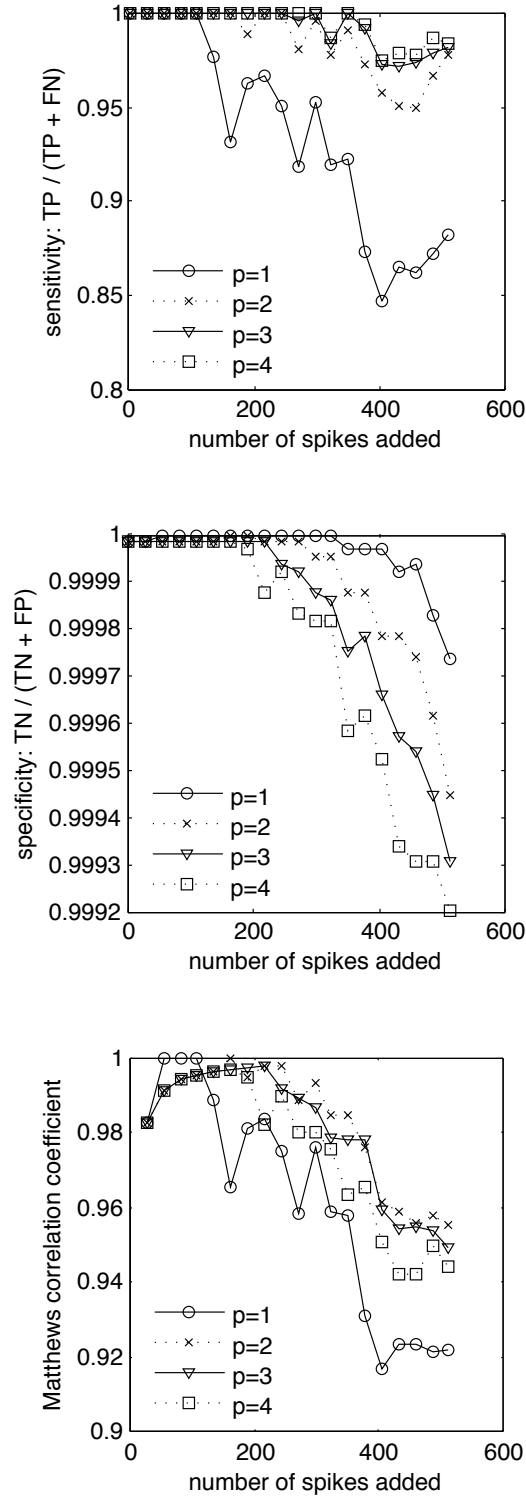


Figure 3: Numerical experiment showing the robustness of the spike detection accuracy to the number of spikes added in the synthetically spiked brain example and to adjustments to the threshold given by Otsu’s method. Each curve with points corresponds to raising the Otsu’s threshold to the specified fractional power ( $1/p$ , where  $p \in \{1, 2, 3, 4\}$ ), and the solid black line is perfect agreement with the number of spikes added (i.e. 100% detection accuracy). Taking the square root of the Otsu threshold ( $p = 2$ ) seems to give the most robust accuracy as the number of spikes increases.

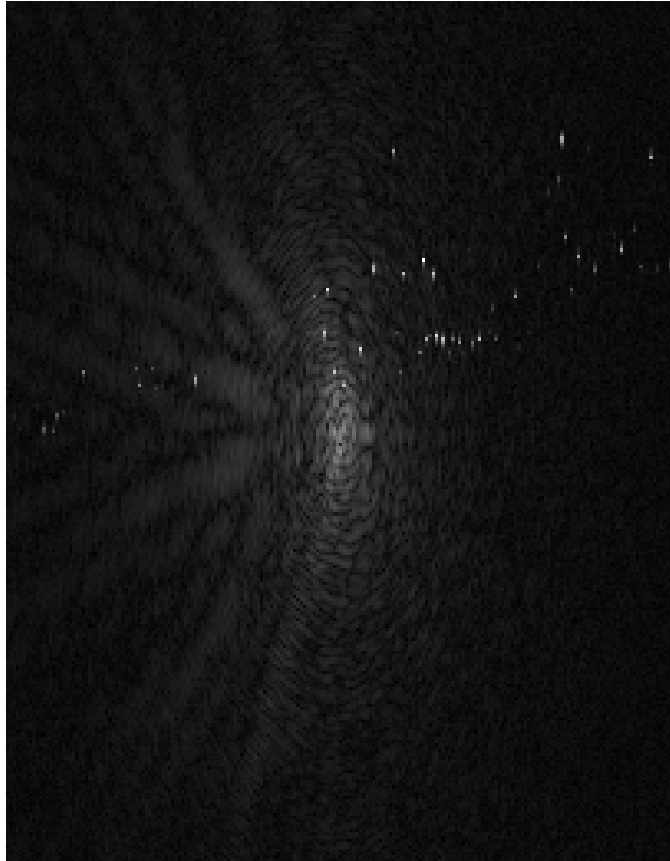


Figure 4: Example of spike corruption in  $k$ -space from the fat-water imaging data set acquired in the *in vivo* experiment. The bright points that don't follow the general pattern of data are almost certainly corrupted. Low intensity features have been scaled up to aid visualization by taking the square root of the magnitude of the coefficients. This is the same data used for the uncorrected images in Fig. 6.

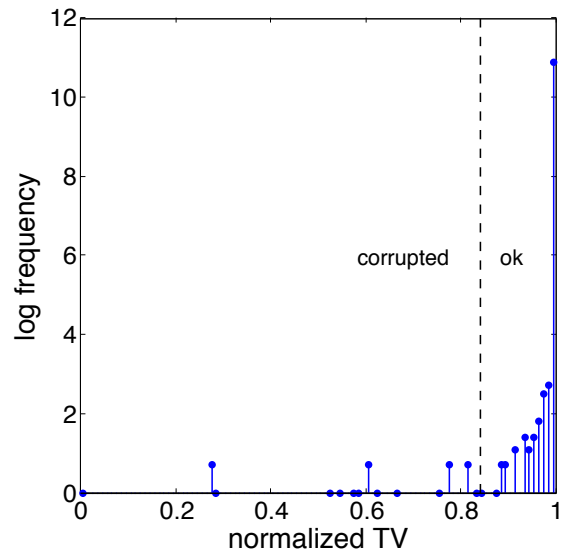


Figure 5: Histogram of normalized total variation for the corrupted fat-water imaging data. The number of spikes is much smaller in this real-world case, but the general characteristics of the histogram are the same. The cutoff obtained using Otsu’s method shows again a good division between the few spikes and the much more numerous non-spike-corrupted data.

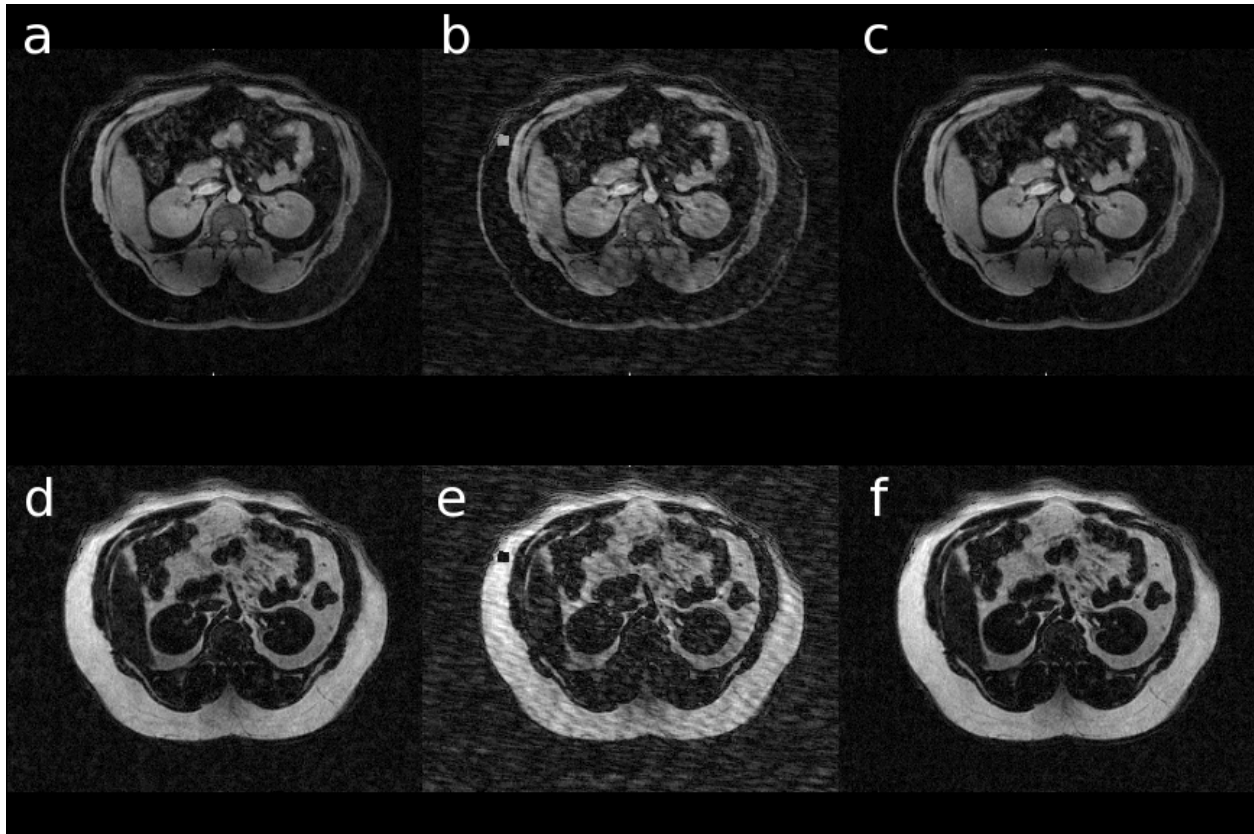


Figure 6: Algorithm performance with an unknown number of spikes in real data acquired with a faulty RF room shield during a whole-body gradient echo scan for fat-water imaging. The upper row (a–c) shows the water images; the lower row (d–f) shows fat images. The original, corrupted data is shown in the center column (b,e). The degradation in image quality is clear, and an area of fat misclassification is visible in the upper left (patient right anterior) of the images. After running this algorithm on the data, the images are significantly cleaned, whether the corrupted data was replaced with zeros (images a, d) or using a compressed sensing reconstruction (c,f). Replacing the spikes with zeros resulted in a 42% artifact level reduction, and the CS reconstruction provided an additional 5% reduction.